The Effects of Cornering Conditions on the Aerodynamic Characteristics of a High-Performance Vehicle and Its Rear Wing

Steven Rijns[a,*], Tom-Robin Teschner[b], Kim Blackburn[a], James Brighton[a]

[a]*Advanced Vehicle Engineering Centre, Cranfield University, Cranfield, MK43 0AL, United Kingdom*
[b]*Centre for Computational Engineering Sciences, Cranfield University, Cranfield, MK43 0AL, United Kingdom*

Abstract

This study investigates the aerodynamic behaviour of a high-performance vehicle and the interaction with its rear wing in straight-line and steady-state cornering conditions. Analyses are performed with Reynolds-Averaged Navier-Stokes (RANS) based computational fluid dynamics (CFD) simulations using a moving reference frame and overset mesh technique, validated against moving ground wind tunnel experiments. Results indicate a significant 20% decrease in downforce and 35% increase in drag compared to straight-line conditions at the smallest considered corner radius of 2.9 car-lengths. Downforce losses primarily stem from performance deficits on the underbody and rear wing, alongside elevated upper body lift. Drag penalties mainly result from additional pressure drag induced by a recirculation wake vortex generated behind the vehicle's inboard side. The vehicle's lateral pressure distribution is also affected, introducing a centripetal force that increases with smaller corner radii. Additionally, analyses of the rear wing reveal alternations of its aerodynamic characteristics in cornering, particularly impacting vortical flow and suction on the lower surface. Throughout the operating conditions, the rear wing's individual downforce contribution falls off beyond its stall angle. At higher angles of attack, the rear wing primarily generates downforce by pressurising the vehicle's upper surfaces, but its interaction with the near-wake leads to a substantially increased pressure drag. Overall, these findings provide crucial insights into the intricate aerodynamic interactions of high-performance vehicles in diverse operating conditions, and form an essential foundation for future research on static and active aerodynamic designs in the pursuit to optimise vehicle performance in dynamic driving conditions.

Keywords:
Aerodynamics, High Performance Vehicles, Corner, Wind tunnel, DrivAer, CFD

1. Introduction

Cornering conditions can have a substantial impact on the aerodynamic performance of ground vehicles. This is especially true for high-performance and racing vehicles, which are equipped with delicate aerodynamic elements that generate downforce to improve tractive forces. Yet, most aerodynamic design evaluations are conducted in straight-line conditions, leading to suboptimal vehicle designs in cornering conditions.

The focus on straight-line conditions in the vehicle aerodynamics research is primarily due to the challenges in replicating cornering conditions in wind tunnel experiments. Experimental techniques capable of recreating some aspects of cornering conditions exist, but they all have limitations in accuracy (Keogh et al. (2015a), Toet (2013)). In contrast, numerical simulations offer complete control over operating conditions and are therefore preferred for cornering analyses.

Previous research examining the influence of steady-state

cornering on the aerodynamics of simplified automotive bodies has consistently shown significant pressure distribution variations compared to straight-line conditions (Keogh (2016), Keogh et al. (2016), Nakashima et al. (2020)). The variation in lateral pressure distribution along the vehicle gave rise to an outboard pressure rise and an inboard pressure drop. The resultant centripetal force and outboard-directed yawing moment demonstrated a linear increase with decreasing corner radii. Conversely, lift generation exhibited a gradual decrease with reduced corner radii, while drag experienced an exponential increase. Notably, the significant rise in drag was primarily attributed to heightened pressure drag and could be related to the formation of a highly asymmetric near-wake structure in cornering conditions.

Research on the DrivAer model (Heft et al. (2012)), a standard benchmark for automotive passenger vehicles, has demonstrated the notable impact of cornering conditions on its aerodynamic features (Josefsson et al. (2018), Nakashima et al. (2015), Kono et al. (2016)). Corresponding with findings on simplified automotive bodies, these studies consistently observed increased pressure on the vehicle's outboard side and decreased pressure on the inboard side compared to straight-line conditions. Additionally, an increasing centripetal force was

*Corresponding author at: Advanced Vehicle Engineering Centre, Cranfield University, Cranfield, MK43 0AL, United Kingdom.
Email address: steven.rijns@cranfield.ac.uk

uniformly noted, although the direction of the yawing moment appeared to be influenced by the vehicle's sideslip angle, aligning with dynamic vehicle motion findings (Okada et al. (2012), Tsubokura et al. (2012)).

Studies on the DrivAer model also highlighted an increase in drag and a slight reduction in lift as corner radii decreased. The heightened drag was primarily accumulated toward the vehicle's rear end and likely affected by the reported asymmetric near-wake structure. Notably, an elevated corner sensitivity was found for open-wheel race cars equipped with downforce-generating aerodynamic elements, since the individual performances of its aerodynamic devices were also affected in cornering conditions (Albukrek et al. (2006)). This is in agreement with simulations on a formula-type car navigating a sequence of corners, which experienced downforce fluctuations of approximately 20% (Nara et al. (2014)).

A common aerodynamic element featured on high-performance and racing vehicles is a rear wing, due to its high adjustability. Research on the effects of rear wings on simplified automotive vehicles in straight-line conditions revealed not only their individual downforce and drag contributions, but also indicated toward secondary interactions with the vehicle and its near-wake impacting the overall aerodynamic performance (Garry and Le Good (2005), Mathur et al. (2021), Buljac et al. (2016)). Analyses on open wheel race cars even demonstrated downforce enhancement effects on the vehicle's underbody due to the interaction with the rear wing (Katz and Dykstra (1989), Katz and Largman (1989)).

Existing findings primarily focused on straight-line analyses, however studies on isolated inverted wings already indicated the significance of yaw and cornering flow conditions on their aerodynamic performance (Keogh et al. (2015b), Gogel and Sakurai (2006)). Additionally, previous research by the current authors also highlighted the importance of yaw conditions on the aerodynamic characteristics of high-performance vehicles equipped with various aerodynamic elements (Rijns et al. (2024b)). These conditions not only influenced individual performances but also interactions between elements and the vehicle body. The vehicle with rear wing configuration proved to be most effective, but also exhibited the highest yaw sensitivity.

Overall, existing literature emphasised the importance of oncoming flow conditions on the aerodynamic performance of vehicles and their aerodynamic elements. However, research predominantly focuses on straight-line conditions, leaving the effects of cornering conditions under explored. This study addresses this gap by analysing the aerodynamic characteristics of a high-performance vehicle and its aerodynamic interaction with a rear wing at varying angles of attack in straight-line and cornering conditions. The findings not only provide a foundational basis for future research on static aerodynamic elements, but also for innovative active solutions which have the potential to further enhance vehicle performance in dynamic conditions (Kurec et al. (2019), Broniszewski and Piechna (2019, 2022),

Piechna et al. (2022), Zavala et al. (2023)). The presented results include aerodynamic force measurements from moving ground experiments in the 8x6 Wind Tunnel at Cranfield University and numerical data sets from Reynolds-Averaged Navier-Stokes (RANS) simulations under varying operating conditions.

2. Methodology

2.1. Vehicle Model

Vehicle aerodynamics research is commonly conducted on generic reference models such as the DrivAer model (Heft et al. (2012)). This study uses the *DrivAer hp-F* model (Soares et al. (2018)), a high-performance variant established on a 35% scale DrivAer Fastback configuration with smooth underbody and rotating wheels. The vehicle model is equipped with an additional 41 mm front bumper splitter, forebody strakes, 10° underbody multichannel diffuser and NACA 6412 profile rear wing. The *DrivAer hp-F* is illustrated in Figure 1 and its parametric dimensions are listed in Table 1.
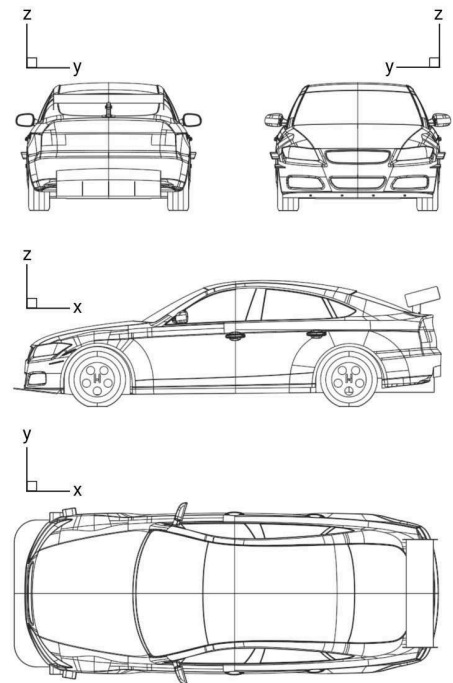

Figure 1: The *DrivAer hp-F* model

Physics of Fluids

AIP
Publishing

Table 1: Parametric dimensions of the *DrivAer hp-F* model

Parameter	Value	
Car scale (CS)	35	%
Length (L)	1.6144	m
Width (W)	0.6273	m
Height (H)	0.4890	m
Ride height (h_o)	0.0455	m
Area (A_{ref})	0.2647	m^2

2.2. Operating Conditions

This study analyses the vehicle's aerodynamic behaviour in straight-line and steady-state cornering conditions with radii of 5.75 and 2.9 car-lengths (L), corresponding to relative airflow yaw angles of respectively 5° and 10° at the front of the vehicle. In the cornering conditions, the vehicle travels at a constant angular velocity ω [rad/s] about the corner's centre, illustrated in Figure 2. The vehicle's position is considered to be tangent to the curved path line through its centre, although this can vary substantially with driving styles (Milliken et al. (1995)). The corner radius R [m] is defined as the distance between the centre of rotation (COR) and the centre of the vehicle.

The velocity of the airflow relative to the vehicle, as well as the relative dynamic pressure, will increase with distance from the centre of rotation. Moreover, the angle of the relative airflow ψ [°] will vary along the vehicle and can be expressed by Eq. (1). Here, x_c and y_c are the coordinates of the centre of rotation. This relationship provides a relative airflow angle at the front of the vehicle of $\psi \approx 5$° for the 5.75L radius corner and $\psi \approx 10$° for the 2.9L radius corner. To approximate steering inputs, the front tyres match these respective relative airflow angles.

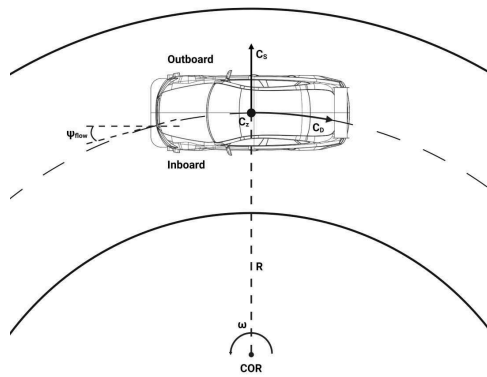$$\psi = tan^{-1}\left(\frac{x - x_c}{y - y_c}\right) \quad (1)$$

Figure 2: Representation of a steady-state cornering condition with indicated aerodynamic force directions

The evaluation of aerodynamic lift and side forces remain in the z-direction and y-direction of the global coordinate system. However, aerodynamic drag is the resistance created by airflow in the direction of the vehicle's motion and therefore varies with the relative airflow angle along the vehicle in cornering conditions (Keogh et al. (2015a)).

2.3. Wind Tunnel Experiments

Wind tunnel tests on the *DrivAer hp-F* model are conducted in the closed return 8x6 Wind Tunnel at Cranfield University (Figure 3). The wind tunnel has a 2.44 m by 1.83 m (8 ft x 6 ft) rectangular test section with corner fillets and is 5.18 m long. The test section is equipped with a 42 mm elevated moving ground facility for synchronous relative air and ground movement speed to prevent the formation of a ground plane boundary layer.

The vehicle model is suspended by an overhead strut system (OS) above a rolling belt (RB), which is 1.2 m wide and 2.75 m long. The wheels are independently supported by wheel supports (WS), and match the rolling belt speed. The facility is also equipped with a two-stage boundary layer suction system to optimise the ground plane boundary layer. The first stage system (BL1) consists of a scoop intake and is positioned 0.73 m upstream of second stage system (BL2), which uses suction through a porous plate just upstream of the rolling belt system. The complete experimental setup on the *DrivAer hp-F* model using the moving ground facility provided a blockage ratio of approximately 9.6%.

Aerodynamic forces and moments are measured on the vehicle with varying rear wing angle of attack settings at a constant wind speed of 40 m/s, corresponding to a Reynolds number of 4.21×10^6. The measurements are conducted with an Aerotech® six-component internal balance, positioned 800 mm downstream of the vehicle's nose and 120 mm above the vehicle's floor. The internal balance has a nominal accuracy of ±0.06% of the full scale measurement range, which gives a
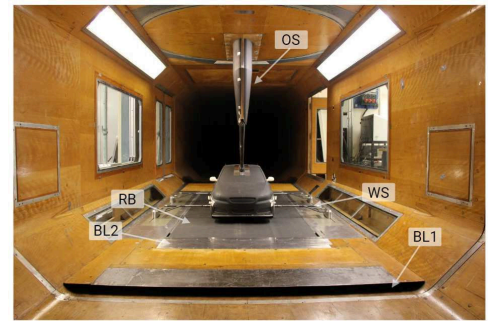

Figure 3: Moving ground experimental setup in the 8x6 Wind Tunnel at Cranfield University

3

measurement accuracy of ±0.90 N for lift and ±0.18 N for drag. The system does not measure forces on the independently supported wheels.

Data acquisition is conducted at a sample rate of 200 Hz over a 10 s time interval. The constant fan rotor speed provides a wind speed variance of less than 0.1 m/s during each acquisition interval. Time-averaged quantities are obtained and converted into non-dimensional force coefficients using Eq. (2). The measured forces are indicated with F_i [N] and the non-dimensional force coefficients with C_i [-], where i is used to indicate lift (L) or drag (D). The measured freestream dynamic pressure in the wind tunnel is indicated by P_{dyn} [Pa] and the vehicle model's reference area by A_{ref} [m^2].

$$C_i = \frac{F_i}{P_{dyn} \cdot A_{ref}} \qquad (2)$$

The data acquisition at each rear wing angle of attack has been repeated three times to assess the repeatability of the experiments. The repeatability at each angle of attack is expressed as the maximum difference between a single measurement and the average of the three repeated runs at that angle. The lowest repeatability across the experimental dataset manifested as a maximum difference of $|\Delta C_L| \approx 9.4e^{-4}$ ($< 0.29\%$) for lift and $|\Delta C_D| \approx 5.2e^{-4}$ ($< 0.17\%$) for drag.

2.4. Numerical Simulations

This study employs numerical simulations to analyse the aerodynamic behaviour of the *DrivAer hp-F* model with a varying rear wing angle of attack in straight-line and cornering conditions within an open road environment. Additionally, simulations replicating the experimental setup in the 8x6 Wind Tunnel at Cranfield University have been performed, which has been demonstrated to be beneficial for validation and correlation purposes (Rijns et al. (2024a)). Both simulation sets are established on the same methodology but executed on different computational domains.

Throughout the analyses in this paper, numerical results of aerodynamic force coefficients, static pressure coefficients and total pressure coefficients are used. The numerical force coefficients are expressed by Eq.(2), and use a reference dynamic pressure based on the air density ρ_{ref} [kg/m^3] and freestream velocity v_{ref} [m/s], as described in Eq.(3)

$$P_{dyn} = \frac{1}{2} \cdot \rho_{ref} \cdot v_{ref}^2 \qquad (3)$$

Static pressure coefficients C_p [Pa] and total pressure coefficients C_{pT} [Pa] are expressed by Eq.(4) and Eq.(5), respectively. Here, P_s [Pa] represents the the static pressure, P_t [Pa] the total pressure, and P_{op} [Pa] the operating pressure of 101325 Pa.

$$C_p = \frac{P_s - P_{op}}{P_{dyn}} \qquad (4)$$

$$C_{pT} = \frac{P_t - P_{op}}{P_{dyn}} \qquad (5)$$

2.4.1. Computational Domain & Boundary Conditions

The present study uses a rectangular domain with modified inlet and outlet positions in combination with a moving reference frame to simulate the straight-line and cornering operating conditions. Previous studies have indicated that this methodology improves the numerical workflow efficiency over using a curved computational domain, since it allows the investigation of various cornering conditions using only one domain (Keogh et al. (2015a, 2016), Okada et al. (2012), Tsubokura et al. (2012)). This *"open road"* computational domain, depicted in Figure 4, adheres to best practice guidelines for automotive aerodynamics simulations (Lanfrit (2005)), with dimensions extending from 3L in front to 5L behind the vehicle. The side and top walls are positioned 1.5L away from the vehicle.

Cornering conditions are simulated with a rotational frame motion about an external point, which acts as the centre of rotation. Straight-line conditions are modelled with a constant translational frame motion to ensure consistency across all operating conditions. The side inlets and outlets are not required for straight-line conditions, which are therefore modelled as symmetry walls to prevent boundary layer growth. Additionally, the ground plane is prescribed to remain stationary relative to the moving reference frame in all operating conditions. Wheel rotation is modelled using moving wall boundary conditions, applying relative angular velocities to achieve the desired tangential velocity at each wheel.

An overview of the setup for each operating condition is provided in Table 2. All conditions are simulated at a (tangential) velocity of 40 m/s, corresponding to a Reynolds Number of 4.29×10^6. To replicate realistic road conditions, turbulence settings are based on on-road turbulence measurements for ground vehicles (Saunders and Mansour (2000)).
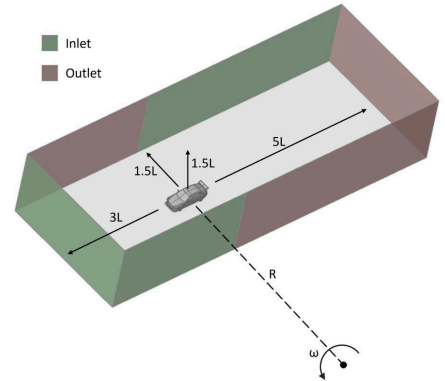

Figure 4: Representation of the *"open road"* computational domain and cornering boundary conditions

Table 2: Numerical settings for each operating condition simulated with the *"open road"* computational domain

Feature	Straight-line	5.75L Radius Corner	2.9L Radius Corner
Impact yaw angle	$\psi \approx 0°$	$\psi \approx 5°$	$\psi \approx 10°$
Moving reference frame			
frame motion	translational	rotational	rotational
motion axis (x, y, z)	1, 0, 0	0, 0, 1	0, 0, 1
velocity	$v = 40$ m/s	$\omega = 4.309$ rad/s	$\omega = 8.544$ rad/s
Inlets & Outlets			
velocity-inlet	$v = 0$ m/s	$v = 0$ m/s	$v = 0$ m/s
pressure-outlet	$P_{gauge} = 0$ Pa	$P_{gauge} = 0$ Pa	$P_{gauge} = 0$ Pa
turbulent intensity	$I = 4\%$	$I = 4\%$	$I = 4\%$
turbulent length scale	$l = 2.5$ m	$I = 2.5$ m	$I = 2.5$ m
Wheels rotation			
rotation axis front (x, y, z)	0, -1, 0	$\sin(\psi)$, -1, 0	$\sin(\psi)$, -1, 0
rotation axis rear (x, y, z)	0, -1, 0	0, -1, 0	0, -1, 0
velocity inboard	$\omega = 363.64$ rad/s	$\omega = 353.73$ rad/s	$\omega = 345.05$ rad/s
velocity outboard	$\omega = 363.64$ rad/s	$\omega = 374.55$ rad/s	$\omega = 386.16$ rad/s
Air properties			
reference density	$\rho_{ref} = 1.204$ kg/m^3	$\rho_{ref} = 1.204$ kg/m^3	$\rho_{ref} = 1.204$ kg/m^3
reference dynamic viscosity	$\mu_{ref} = 1.813e^{-5}$ kg/(m s)	$\mu_{ref} = 1.813e^{-5}$ kg/(m s)	$\mu_{ref} = 1.813e^{-5}$ kg/(m s)
reference temperature	$T = 293$ K	$T = 293$ K	$T = 293$ K

As previously mentioned, simulations are also conducted on a numerical representation of the 8x6 Wind Tunnel at Cranfield University, illustrated in Figure 5, to facilitate validation and correlation efforts. The *"wind tunnel"* computational domain extends 3L in front and 5L behind the vehicle model as well, resulting in a total domain length of 14904 mm. Cross-sectional dimensions match the 2438 mm width and 1787 mm height of the physical wind tunnel.

Airflow conditions from the wind tunnel experiments are approximated with a velocity-inlet condition using a constant velocity of 40 m/s, a turbulent intensity of 0.05%, and a turbulent viscosity ratio of 10. Reference air properties are based on averaged temperature and dynamic pressure recording across all measurements, providing a density of 1.178 kg/m^3, a dynamic viscosity of 1.808e^{-5} kg/(m s), and a temperature of 292 K.
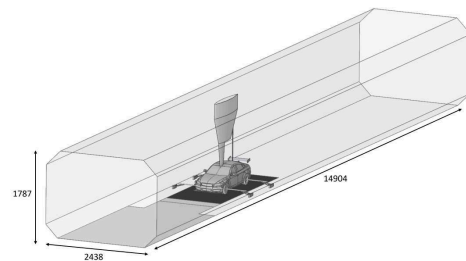

Figure 5: Computational wind tunnel domain

Geometric representations of the overhead support system and wheel supports are included to match the approximated experimental blockage ratio of 9.6%. The rolling belt is simulated using a translational moving wall condition of $v = 40$ m/s on the wall section depicted in black. Rotating wheels are modelled with rotational moving wall conditions of $\omega = 363.636$ rad/s to align with the tangential velocity of the rolling belt. Lastly, the floor upstream of the two-stage boundary layer suction system, depicted in grey, is modelled as a symmetry wall to approximate boundary layer control.

2.4.2. Mesh

The computational domain is constructed with five unstructured poly-hexcore meshes using an overset mesh methodology in ANSYS Fluent Meshing. The overset mesh technique interpolates cell data in overlapping mesh regions, enabling targeted mesh transformation without the requirement to remesh the entire domain. This technique has demonstrated effectiveness in automotive applications (Szudarek and Piechna (2021)) and is therefore deployed to improve the numerical workflow efficiency in this study, which involves simulations of 48 vehicle configurations.

The overset mesh strategy employs four component mesh zones, illustrated in Figure 6, overlaid on a background mesh which covers the entire domain including refinement zones. The grey overset interface contains the vehicle model and rear wheels. The blue overset interfaces include the front wheels and enable steering input adjustments based on corner radius. The green overset interface confines the rear wing, facilitating control over its angle of attack.
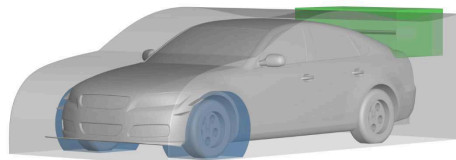
5

Figure 6: Overset component mesh interfaces

The present mesh settings are based on established guidelines from previous work (Rijns et al. (2024a)), where grid convergence levels and near-wall modelling approaches for practical RANS simulations on high-performance vehicles were evaluated against experimental data and high-fidelity Delayed Detached Eddy Simulations (DDES) on a wall-resolved mesh with $y^+ < 1$. Based on the Grid Convergence Index (GCI) results of $GCI_{32} = 0.47\%$ and $GCI_{21} = 0.04\%$ for lift coefficients, obtained from coarse (3), medium (2) and fine (1) grids, the study recommended the mesh strategy for the medium grid.

Accordingly, this study uses base element and vehicle surface element sizes of approximately 7.25% and 0.45% of the vehicle's length, respectively. Local element sizes on aerodynamic elements are reduced to about 2.5% of the vehicle's length and to about 0.25% on small geometric features. The vehicle model is prepared with a medium near-wall treatment, targeting a $y^+ \approx$ 120-150 with around 4-6 inflation layers. Additionally, refinement zones with gradually increasing element sizes are implemented to offer increased resolution in the vehicle's near-field and wake region for each operating condition, as shown in Figure 7.

Overall, this mesh strategy yields a total cell count of approximately 15.1 million cells for the *"open road"* computational domain, with zero orphan cells and 99% of the cells with an orthogonal quality above 0.66. The same strategy is applied to
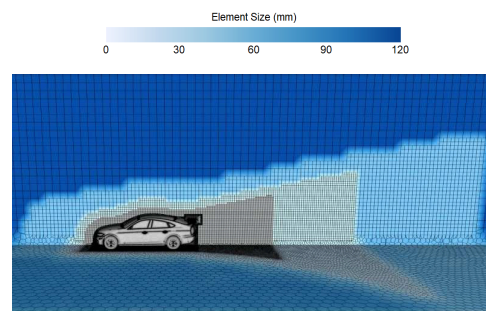

Figure 7: Contour plot of element sizes on the region in proximity of the vehicle in the *"open road"* domain using a volume slice at y = 0 (symmetry)

the *"wind tunnel"* computational domain, resulting in a total cell count of around 19.2 million cells with zero orphan cells and 99% of the cells with an orthogonal quality above 0.61.

2.4.3. Solver

Steady-state RANS simulations using the k-ω SST turbulence model (Menter (1994)) with standard settings in ANSYS Fluent are conducted in this study. The k-ω SST model is selected for its proven cost-effectiveness for aerodynamic simulations on the *DrivAer hp-F* model in a previous study, which assessed the predictive capabilities of various RANS models against high-fidelity DDES simulations and experimental data (Rijns et al. (2024a)).

Along with the transport equations, the continuity and momentum equations are solved. Spatial discretisation is performed using the second order upwind scheme and pressure-velocity coupling is conducted using the coupled scheme. Initial trade-off efforts between simulation duration and statistical convergence of the vehicle's lift and drag coefficients determined a total duration of 750 iterations. Statistical convergence, defined as the point at which the moving mean of the monitored force coefficients stabilised, was typically reached within 400 iterations. The presented force coefficients are therefore averaged over the last 250 iterations.

The simulations were performed on two AMD EPYC 7543 CPUs using a total of 64 cores. On average, the simulations required approximately 5 hours and 30 minutes of computation time on the *"open road"* domain, and around 4 hours on the *"wind tunnel"* domain.

3. Validation & Correlation

This section validates the numerical methodology against experimental data and analyses differences between wind tunnel and open road conditions for correlation. Validation is based on agreement between force data on the vehicle body from the experiments (Exp) and simulations on the computational wind tunnel domain (WT), presented in Figure 8. Detailed analyses of the results will be provided in section 4.

The simulations overpredict downforce by $\Delta C_L \approx$ -0.028 (+10%) in the 0°–12.5° angle of attack range, with an average relative deviation of $|\Delta C_L| \approx 0.004$ (2%). Beyond the rear wing's stall angle of approximately 12.5°, most downforce from the rear wing is generated by its interaction with the vehicle body. While some discrepancies are present in the transition just beyond the stall angle, the simulations provide a steady downforce underprediction of $\Delta C_L \approx 0.009$ (-2%) along the 17.5°–27.5° range, with an average relative deviation of $|\Delta C_L| \approx 0.005$ (1%). Furthermore, the simulations underpredict drag on average by $\Delta C_D \approx$ -0.025 (-8%), with an average relative deviation of $|\Delta C_D| \approx 0.002$ (<1%) across the angle of attack range.
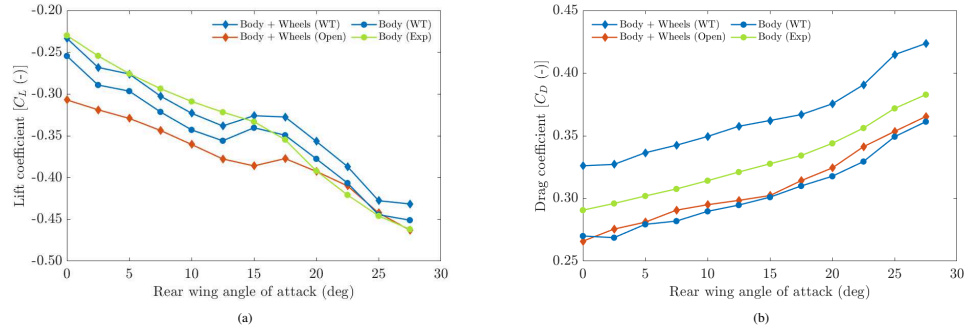
Figure 8: (a) Lift coefficients and (b) drag coefficients results from the experiments (Exp), 'wind tunnel' simulations (WT), and 'open road' simulations (Open)

Aerodynamic forces on the wheels were excluded in the wind tunnel experiments, but the simulation results from the computational wind tunnel domain (WT) indicate that their inclusion reduces total downforce by $\Delta C_L \approx 0.019$ (-6%) and increases total drag by $\Delta C_D \approx 0.06$ (+20%). The inclusion of wheel forces manifests as nearly invariant offsets, with average relative deviations of $< 1\%$ for both forces across the angle of attack range, suggesting they do not influence experimental force trend analyses in this study.

The simulated force data from the *"open road"* and *"wind tunnel"* domains show expected absolute force offsets attributable to wind tunnel conditions such as blockage and interference effects. However, there are also noticeable relative gradient variations, particularly across the 17.5°–27.5° angle of attack range. Figure 9 illustrates that these force offsets are primarily influenced by reductions in upper surface pres-

sure associated with locally increased airflow velocities in the *"wind tunnel"* domain, consistent with prior research (Rijns et al. (2024a)). Moreover, the rate at which the rear wing's pressurisation affects the vehicle's upper surfaces is shown to be influenced, contributing significantly to the variations in force gradients.

Overall, strong agreement between numerical and experimental force trends provides confidence in the accuracy of the numerical methodology. The correlation results provide insights into the effects of wheel forces and experimental conditions on the vehicle's aerodynamic characteristics, supporting interpretation of the experimental data.
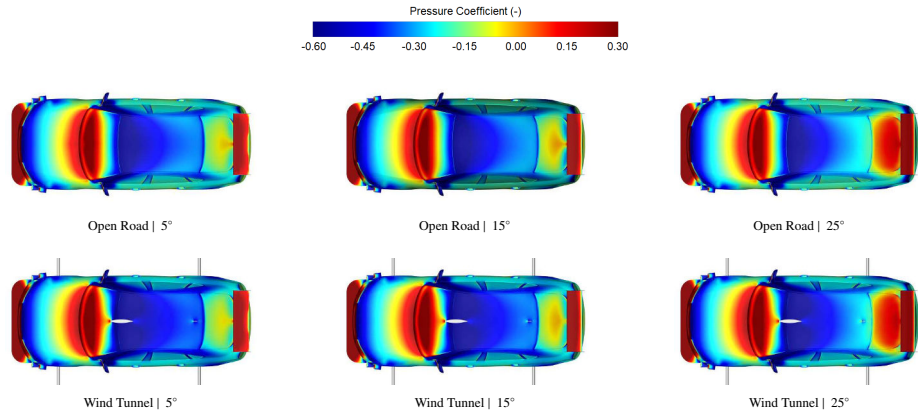

Figure 9: Comparison between the pressure coefficient distribution on the vehicle in the 'open road' and 'wind tunnel' domain with varying rear wing angle of attack. The overhead balance system present in the 'wind tunnel' domain is not displayed for improved visibility.

4. Results & Discussions

This section analyses the aerodynamic behaviour of the vehicle with various rear wing angle of attack settings in the straight-line, 5.75L radius corner, and 2.9L radius corner conditions. Initially, the overarching influence of these operating conditions on downforce and drag performance is discussed. Subsequently, detailed analyses of surface pressure and wake characteristics are provided to further clarify the observed force trends. Finally, aerodynamic characteristics and interactions involving the rear wing are investigated. Throughout the presentation of results, the "outboard side" in cornering conditions refers to the right side of the vehicle, with clarification provided in figure descriptions if uncertain from the presented view.

4.1. Aerodynamic Forces

Downforce and drag performances from the total vehicle and rear wing individually are presented in Figures 10 and 11. To enhance data visualisation and trend analyses, these results have been smoothened using the *'Lowess'* local regression method in MATLAB with a span of five data points.

In the straight-line condition, the vehicle's downforce performance generally increases with $\Delta C_L \approx -0.014$ per 2.5° angle of attack increment within the initial 0°–12.5° downforce enhancement region. Subsequent to a minor force plateau between 12.5° and 17.5°, the downforce gain rises by approximately 47% to $\Delta C_L \approx -0.020$ per 2.5° angle of attack increment in the following 17.5°–27.5° downforce enhancement region.

Downforce generated on the rear wing significantly contributes to the vehicle's initial total downforce enhancement region, but rapidly decreases after its stall angle of approximately 12.5°. However, the vehicle's total downforce continues to increase, suggesting the rear wing has additional effects on the vehicle's aerodynamic performance which will be explored later.

In the 5.75L radius corner condition, the vehicle experiences a drop of about $\Delta C_L \approx 0.022$ (-7%) in downforce performance at low angles of attack compared to straight-line conditions. At higher angles of attack however, downforce losses diminish and the vehicle generates on average $\Delta C_L \approx -0.012$ (+3%) more downforce than in straight-line conditions. The rear wing exhibits a noticeable corner sensitivity, with a $\Delta C_L \approx 0.007$ (-4%) drop in downforce performance before its stall angle. The corner sensitivity diminishes beyond the stall angle, where downforce performance is primarily influenced by the pressure build-up on the rear wing's upper surface.

In the 2.9L radius corner condition, the vehicle's total downforce performance within the 0°–12.5° range has decreased by approximately $\Delta C_L \approx 0.065$ (-19%) compared to the straight-line condition and by $\Delta C_L \approx 0.050$ (-14%) compared to the 5.75L radius corner condition. Along the 17.5°–27.5° range, the downforce performance depicts a reduced sensitivity to angle of attack increments. The rear wing's individual downforce performance has decreased by about $\Delta C_L \approx 0.016$ (-9%) compared to the straight-line condition and by $\Delta C_L \approx 0.009$ (-5%) compared to the 5.75L radius corner condition. Its stall angle is however delayed by about 5° and thereby also defers the downforce drop off at higher angles of attack.

Regarding the vehicle's drag performance, total drag in straight-line conditions increases by $\Delta C_D \approx 0.006$ per 2.5° angle of attack increment within the 0°–12.5° range. The drag penalty grows by over 90% to $\Delta C_D \approx 0.012$ at higher angles of attack. The rear wing's drag production increases at an increasing rate throughout the angle of attack range. Yet, its contribution to the vehicle's total drag penalty only reaches about 70%. This indicates that the rear wing has additional interactions with vehicle's flow field which produce drag and will be investigated later.

In the 5.75L radius corner condition, the vehicle generates on average $\Delta C_D \approx 0.057$ (+19%) more drag compared to straight-
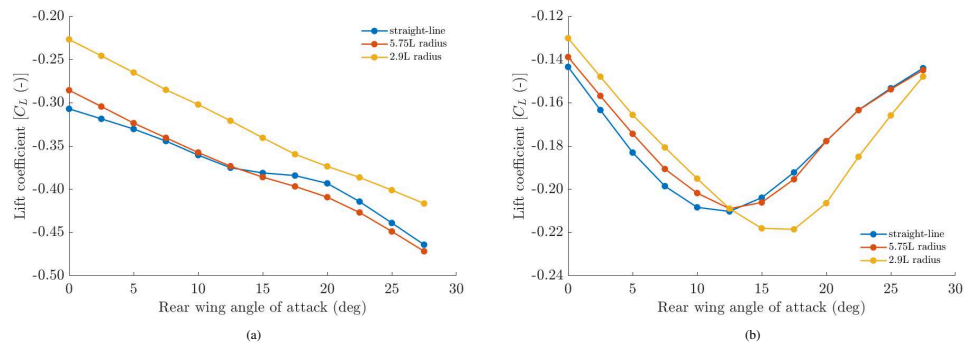

Figure 10: Lift coefficients on the (a) entire vehicle and (b) rear wing individually as a function of angle of attack in straight-line and cornering conditions
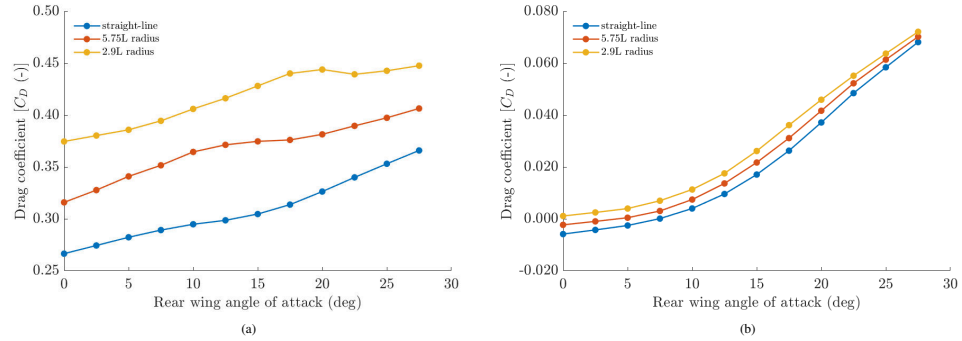
Figure 11: Drag coefficients on the (a) entire vehicle and (b) rear wing individually as a function of angle of attack in straight-line and cornering conditions

line conditions. The initial $\Delta C_\mathrm{D} \approx 0.012$ drag penalty per 2.5° angle of attack increment within the 0°–10° range reduces by about 32% to $\Delta C_\mathrm{D} \approx 0.008$ at higher angles of attack after a small force plateau. The rear wing's drag production has steadily increased by approximately $\Delta C_\mathrm{D} \approx 0.036$ throughout the angle of attack range relative to straight-line conditions.

In the 2.9L radius corner condition, the vehicle's total drag increases non-linearly within the 0°–17.5° range and subsequently plateaus at higher angles of attack. On average, total drag increased by approximately $\Delta C_\mathrm{D} \approx 0.108$ (+35%) compared to straight-line conditions and by $\Delta C_\mathrm{D} \approx 0.050$ (+14%) compared to the 5.75L radius corner condition. The rear wing's drag production also increased by around $\Delta C_\mathrm{D} \approx 0.007$ compared to straight-line conditions and by $\Delta C_\mathrm{D} \approx 0.004$ compared to the 5.75L radius corner condition.

4.2. Vehicle Aerodynamics

This section analyses the vehicle's aerodynamic characteristics in each operating condition to further elaborate on the previously observed force coefficient trends. A comparison of the vehicle's surface pressure distribution is provided in Figures 12-14.

In straight-line conditions, the vehicle's nose exhibits a stagnation zone, followed by sharp airflow acceleration around the its curvature. The associated low-pressure region recovers toward a high-pressure region at the windscreen. More low-pressure regions are observed along the a-pillars and roof's leading edge. The succeeding gradual pressure recovery along the roof becomes much steeper at the slant, influenced by pressurisation from the rear wing.

Cornering conditions cause the high-pressure regions on the vehicle's nose and windscreen to concentrate progressively toward the inboard side with decreasing radii. The pressure across the a-pillars and roof's leading edge increases gradually

on the outboard side but decreases on the inboard side. Conversely, as the yaw angle of the relative airflow reverses downstream of the vehicle's centre, pressure along the roof-lines and c-pillars decreases on the outboard side and increases on the inboard side. Additionally, the relative airflow's increasing yaw angle at the rear of the vehicle shifts the pressure recovery along the slant progressively outboard.

The pressure distribution on vehicle's underbody in straight-line conditions indicates the formation of a separation bubble behind the splitter's sharp leading edge, accompanied by high-pressure regions on either side due to airflow interaction with the inclined splitter surface. Ground clearance is at minimum in between the front wheels, providing a strong venturi effects, evident from the significant low-pressure region around the front axle. The pressure recovers along the centre of the underbody, before airflow is accelerated toward the diffuser inlet. The diffuser provides a gradual pressure recovery, with localised low-pressure concentrations resulting from vortex flow at the diffuser channel separators.

More airflow interacts with the inboard side of the splitter in cornering conditions, resulting in a localised increase in pressure. The curved path also causes the splitter's separation bubble to shift with the relative airflow direction. In the 5.75L radius corner condition, a modest inward propagation of the inboard front wheel is evident alongside the low-pressure region around the front axle. This wheel wake becomes more prominent in the 2.9L radius corner condition and the inboard front wheel itself starts to impose interference effects, hindering front axle downforce generation.

Downstream at the underbody, cornering conditions lead to a progressive pressure decrease ahead of the inboard rear wheel and an increase ahead of the outboard rear wheel. In the 5.75L radius corner, there is a noticeable pressure rise on the outboard side of the diffuser, attributed to interference from the outboard front and rear wheel wakes extending into the diffuser. In the
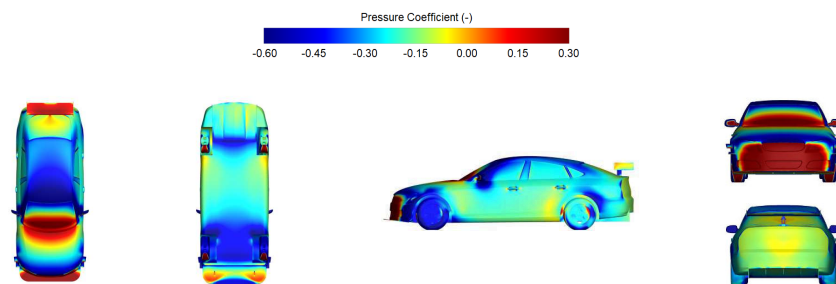
9

Figure 12: Pressure coefficient distribution on the vehicle in straight-line conditions with a 0° rear wing angle of attack
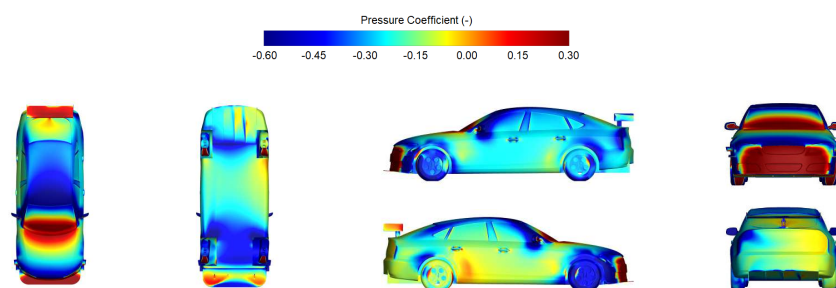

Figure 13: Pressure coefficient distribution on the vehicle in a 5.75L radius corner with a 0° rear wing angle of attack
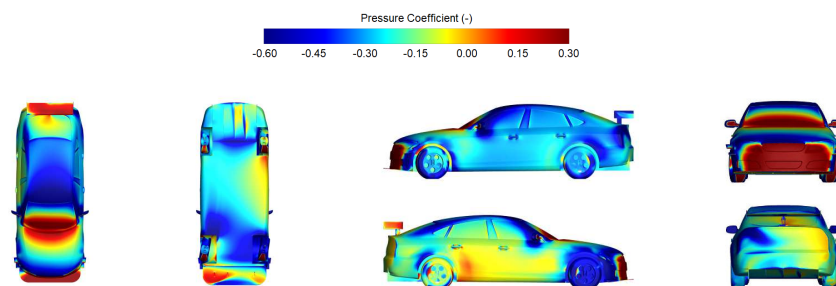

Figure 14: Pressure coefficient distribution on the vehicle in a 2.9L radius corner with a 0° rear wing angle of attack

10

2.9L radius corner, the larger steering input and path curvature prevent the outboard front wheel wake from reaching the diffuser, resulting in a more prominent low-pressure region at the outboard side of the diffuser inlet. However, the curved relative airflow still induces the outboard rear wheel wake across the diffuser, causing downforce losses. Additionally, cornering conditions enhance vortex formation at the diffuser's separators, as indicated by increased low-pressure concentrations in the diffuser channels. Management of the inboard rear wheel wake is also improved, evident from the reduced pressure on the inboard side of the diffuser compared to the straight-line condition.

The vehicle's side panels in straight-line conditions exhibit low-pressure regions extending from the nose to the front wheels, with additional low-pressure regions along the a-pillars, rooflines and c-pillars. The pressure remains relatively consistent along the doors and windows, but reduces around the rear quarter panels. The low-pressure concentrations on the downstream edges of the rear quarter panels are caused by airflow rolling into recirculation zones behind the vehicle, also evident from the associated low-pressure regions on either side of the vehicle's base.

The pressure across the outboard door panels and windows gradually increases in cornering conditions with reducing radii, while the pressure on the outboard roof-line and c-pillar noticeably decreases. Conversely, the pressure across the inboard door panels and windows progressively decreases, while the pressure on the inboard c-pillar slightly increases. The inboard rear quarter panel experiences a significant pressure reduction compared to straight-line conditions, especially around its downstream edge. Overall, these variations induce an inboard acting side force of $\Delta C_S \approx 0.107$ in the 5.75L radius corner condition and $\Delta C_S \approx 0.138$ in the 2.9L radius corner condition.

The pressure across the inboard side of the vehicle's base reduces significantly in cornering conditions, leading to increased pressure drag. This pressure reduction is associated with the intensified formation of inboard recirculation wake vortices, also suggested by the previously identified reduced pressure across the inboard rear quarter panel. These low-pressure traces extend further inward with decreasing corner radii due to en-

hanced wake circulation promoted at high relative airflow curvatures.

Investigation of the wake structure, presented in Figure 15, reveals substantial differences between straight-line and cornering conditions. In the straight-line condition, a distinct recirculation zone forms behind the vehicle's body, accompanied by rear wheel wakes. In cornering conditions, the wake becomes increasingly asymmetric with decreasing radii. The inboard rear wheel wake slightly reduces in size and shifts outward, lessening its impact on the diffuser as previously observed. Conversely, the outboard rear wheel wake enlarges significantly and extends inward, leading to downforce losses on the diffuser's outboard side.

The recirculation wake vortex structure, originating behind the inboard rear quarter panel, is evident in the upper-wake region in cornering conditions. This structure initially develops predominantly in the spanwise direction near the vehicle's base, but it subsequently merges with higher energy airflow from the vehicle's outboard side, forming a dominant streamwise wake vortex. The circulation from this wake structure creates an inboard inwash of high-energy freestream airflow, aiding in the dissipation of pressure losses.

A closer examination of the wake characteristics in cornering conditions, depicted in Figure 16, indicates that the strength of the recirculation wake vortex intensifies with decreasing corner radii. This is evident from the concentration of lower total pressure behind the inboard side of the vehicle's base at the z = 210 mm plane. Smaller corner radii also position the subsequent streamwise wake vortex structure further toward the inboard side, shown by the location of the downstream low total pressure traces. Overall, the magnitude and downstream development of pressure losses on the z = 210 mm plane are most pronounced for smaller corner radii.

At the z = 130 mm plane, a notable inboard inwash effect from the streamwise wake vortex is observed. The resultant crossflow from the inboard to the outboard side of the wake strengthens with decreasing corner radii. This inwash effect energises the wake with high-energy freestream airflow and accordingly mitigates some of the pressure losses from the outboard rear wheel wake at this plane.
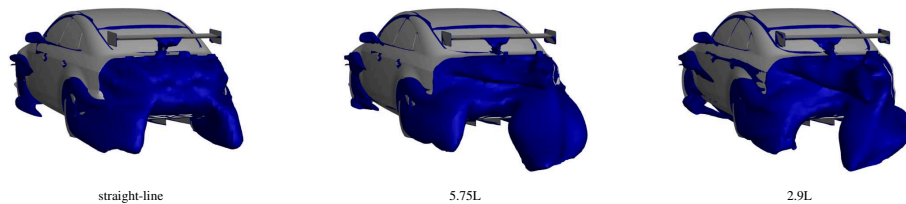

straight-line   5.75L   2.9L

Figure 15: Wake structure visualisations using iso-surfaces of zero total pressure for the vehicle with a 0° rear wing angle of attack in straight-line and cornering conditions
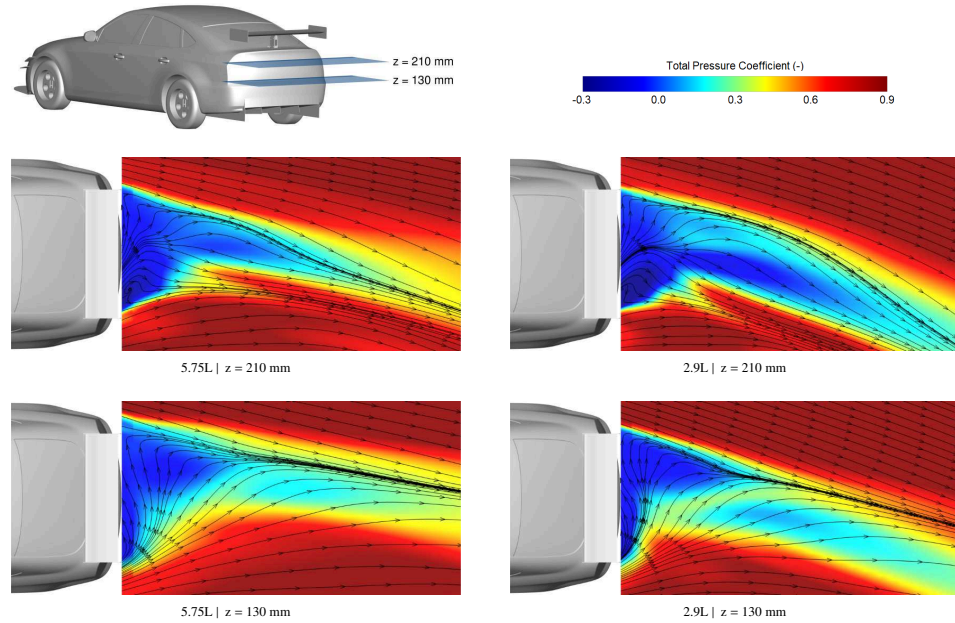
Figure 16: Total pressure coefficient distribution with additional streamlines on wake planes behind the vehicle in cornering conditions. The wake plane positions are illustrated on the top left corner of the figure.

4.3. Rear Wing Aerodynamics

This section investigates the aerodynamic characteristics of the rear wing across a wide angle of attack range in each operating condition. The effects of operating conditions on the vortical flow are first considered to support subsequent analyses of surface pressure data.

Pressure differentials across the endplates drive vortical flow at the rear wing's upper and lower surfaces, as shown in Figure 17. Vortices labelled O_U and I_U form on the outboard and inboard sides of the upper surface, respectively. Similarly, vortices labelled O_L and I_L form on the outboard and inboard sides of the lower surface, respectively.

In straight-line conditions, the pressure differential induces outward-rotating O_U and I_U vortices, and inward-rotating O_L and I_L vortices. A larger pressure differential is present at the lower surface, creating more pronounced O_L and I_L vortices compared to the O_U and I_U vortices at the depicted 0° angle of attack.

Cornering conditions create a pressure build-up on the outside of the outboard endplate, which increases with decreasing corner radii. The altered pressure differential induces an inward-rotating O_U vortex and enhances the O_L vortex. The

pressure on the inside of the inboard endplate is also increased, strengthening the I_U vortex. Additionally, the pressure differential driving the I_L vortex is reduced due to the low-pressure region emerging on the inboard rear quarter panel in cornering conditions.

The pressure distribution on the rear wing's upper surface, illustrated in Figure 18, demonstrates a high-pressure region behind leading edge that gradually diminishes toward the trailing edge. In straight-line conditions, the distribution is symmetrical and pressure increases with angle of attack. However, local pressure reductions occur near the endplates due to airflow spillage from the O_U and I_U vortices.

In cornering conditions, a noticeable pressure reduction is initially observed near the outboard endplate at low angles of attack compared to straight-line conditions, attributed to the inward rotation of the O_U vortex. As the angle of attack increases, the pressure rise across the upper surface mitigates the inward rotation of the O_U vortex and its associated pressure reduction. Nonetheless, flow obstruction from the outboard endplate continues to cause relatively lower pressure behind it at higher angles of attack.
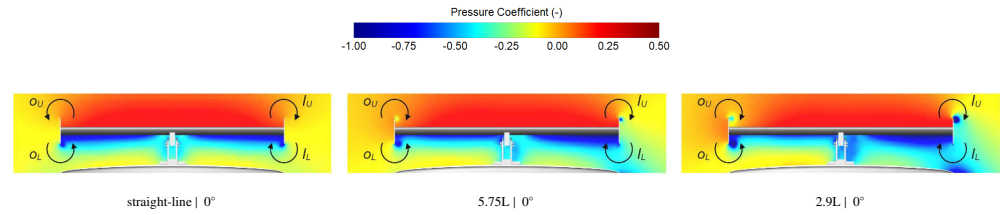
12

Figure 17: Pressure coefficient distribution on a frontal plane (x = 1.25 m) at the rear wing with labelled vorticity for the vehicle with a 0° rear wing angle of attack in straight-line and cornering conditions. The left side of the presented view is the outboard side in cornering conditions.

The rear wing's lower surface exhibits a significant low-pressure region near the leading edge curvature which gradually recovers toward the trailing edge, as depicted in Figure 19. In straight-line conditions, the low-pressure region near the leading edge curvature is initially most substantial across the centre section at 0°, indicating a locally increased effective angle of attack due to downwards induced airflow along the vehicle's body. Suction near the leading edge, as well as the pressure recovery gradient, increases with angle of attack up to the stall angle around 12.5°-15°, beyond which severe flow separation negatively impacts downforce performance. The pressure recovery remains most gradual near the endplates, attributed to the low pressure generated by the O_L and I_L vortices, which is observable even beyond the stall angle.

In cornering conditions, suction near the leading edge curvature initially increases on the inboard side but decreases on the outboard side at 0°, indicating a favourable inboard relative airflow alignment. However, suction across the outboard side noticeably increases at higher angles of attack, while suction on the inboard side starts to decay due to interference from the rear wing support. The increased suction is attributed to the enhanced interaction of the rear wing with faster moving outboard relative airflow as its leading edge nears the vehicle body, along with the increasing strength and flow inducement effects of the O_L vortex at higher angles of attack. Additionally, the strengthening of the O_L vortex and suppression of the I_L vortex in reducing corner radii are evident from the dominant low pressure traces near the outboard endplate and absence of low pressure traces near the inboard endplate across the angle of attack range.

4.4. Rear Wing Interaction

This section investigates the aerodynamic interaction between the rear wing and the vehicle's flow field in each operating condition, building upon previous discussions highlighting the rear wing's significant influence on the vehicle's overall aerodynamic performance, even at angles of attack beyond its stall angle.
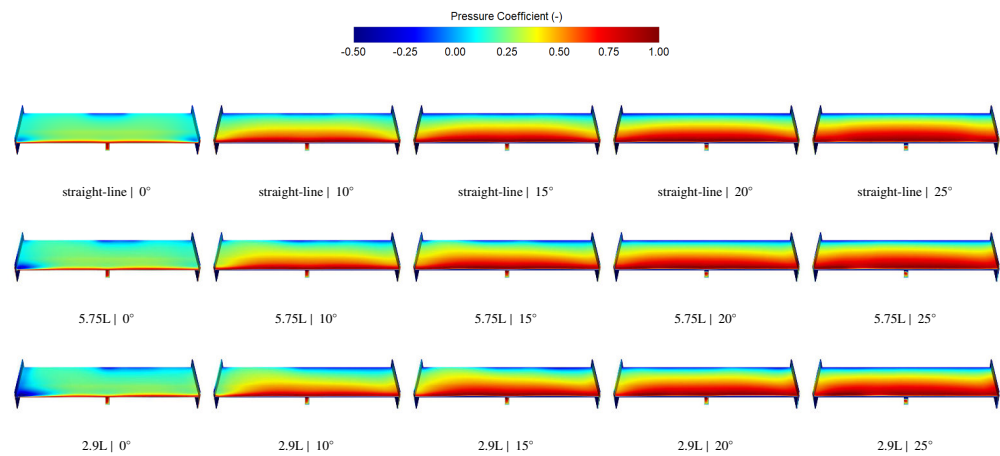

Figure 18: Pressure coefficient distribution on the upper surface of the vehicle's rear wing at various angles of attack in straight-line and cornering conditions. The left side of the presented view is the outboard side in cornering conditions.
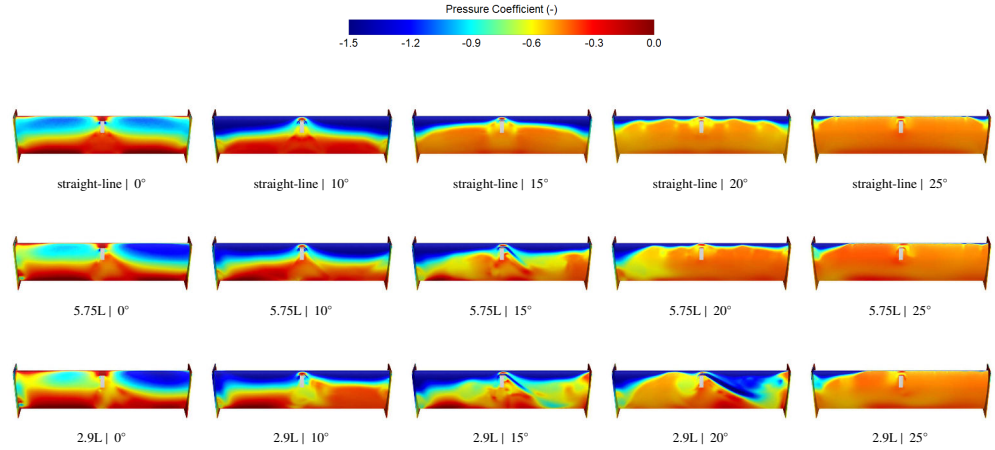
13

Physics of Fluids

Figure 19: Pressure coefficient distribution on the lower surface of the vehicle's rear wing at various angles of attack in straight-line and cornering conditions. The left side of the presented view is the outboard side in cornering conditions.

The rear wing initially creates a modest pressurisation onto the slant at 0°, which is located further outboard at smaller corner radii, as shown in Figure 20. The pressurisation magnitude and subsequent pressure rise along the roof increase gradually with angle of attack increments before the stall angle. Suction underneath the rear wing at these angles of attack casts a low-pressure region onto the vehicle's body. This enhances airflow velocity along the c-pillar pair in straight-line conditions and along the outboard c-pillar in cornering conditions, reducing local pressure. Overall, the aerodynamic interaction causes on average a maximum $\Delta C_L \approx 0.007$ (+1.5%) increase in lift on the slant and roof surfaces just before the rear wing's stall angle in each operating condition.

Beyond the rear wing's stall angle, suction on the lower surface diminishes while pressure on the upper surface keeps increasing, as previously observed. The emitted low-pressure region from the rear wing onto the vehicle's body therefore disappears whereas pressurisation onto the slant and roof significantly increases, shifting inward with decreasing corner radii. Altogether, the aerodynamic interaction at higher angles of attack decreases lift along the slant and roof surface, with an averaged maximum of $\Delta C_L \approx -0.105$ (-24%) reached at the highest angle of attack of 27.5° in each operating condition.

Interaction between the rear wing and airflow toward the vehicle's rear-end and near-wake is also identified. In straight-line conditions, the rear wing's enhanced suction and vortical flow at angles of attack before stall augments recirculation behind the vehicle. This is indicated by reduced pressure traces on the vehicle's base surface, increasing its local drag by $\Delta C_D \approx 0.017$ (+30%) right before the stall angle compared to 0°. Beyond the rear wing's stall angle, strong airflow recirculation, and en-

hanced O_U and I_U vortices further amplify recirculation behind the vehicle, causing a maximum $\Delta C_D \approx 0.047$ (+84%) drag increase on the vehicle's base surface at the maximum 27.5° angle of attack compared to 0°.

In cornering conditions, the rear wing's suction and I_U vortex strength progressively increase with angles of attack before stall, enhancing the inboard recirculation wake vortex and its associated pressure losses. Consequently, drag on the vehicle's base surface increases by $\Delta C_D \approx 0.027$ (+35%) in the 5.75L radius corner condition and by $\Delta C_D \approx 0.023$ (+23%) in the 2.9L radius corner condition right before their respective stall angles compared to 0°. Beyond the stall angle, dominant airflow recirculation behind the rear wing and the further intensified I_U vortex feed the recirculation wake vortex and induce it toward the top inboard corner of the vehicle's base, indicated by the associated low pressure trace locations. Consequently, drag on the vehicle's base surface increases by $\Delta C_D \approx 0.037$ (+48%) in the 5.75L radius corner condition and by $\Delta C_D \approx 0.026$ (+25%) in the 2.9L radius corner condition at the maximum 27.5° angle of attack compared to 0°.
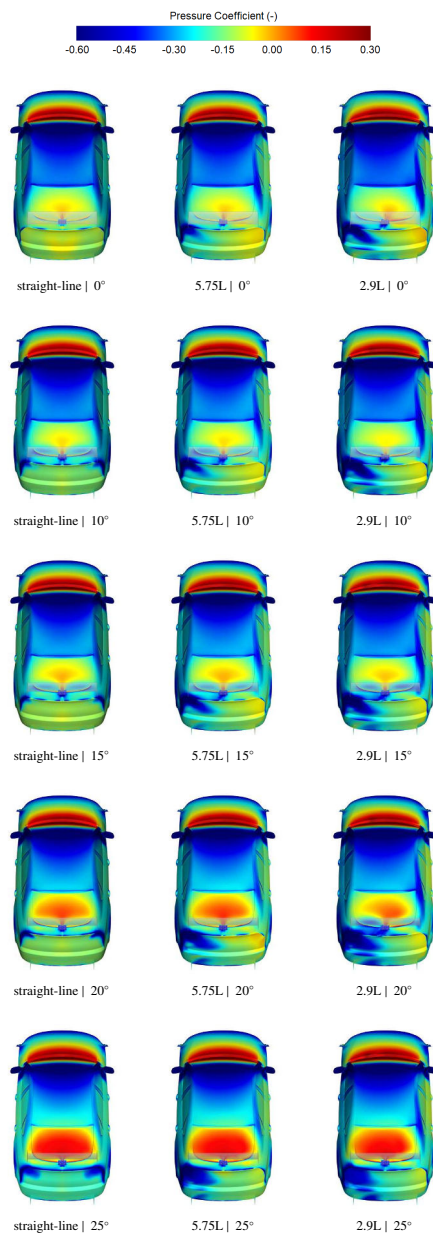
14

Pressure Coefficient (-)

-0.60   -0.45   -0.30   -0.15   0.00   0.15   0.30

straight-line | 0°   5.75L | 0°   2.9L | 0°

straight-line | 10°   5.75L | 10°   2.9L | 10°

straight-line | 15°   5.75L | 15°   2.9L | 15°

straight-line | 20°   5.75L | 20°   2.9L | 20°

straight-line | 25°   5.75L | 25°   2.9L | 25°

Figure 20: Pressure coefficient distribution on the vehicle with varying rear wing angle of attack in straight-line and cornering conditions

5. Conclusions

This study investigated the aerodynamic behaviour of a high-performance vehicle with varying rear wing angle of attack in straight-line and cornering conditions. The analyses were performed on the *DrivAer hp-F*, a high performance variant of the standard DrivAer Fastback configuration. The numerical methodology was validated against aerodynamic force measurement results from moving ground experiments in the 8x6 Wind Tunnel at Cranfield University.

Cornering conditions adversely impacted both the vehicle's overall downforce and drag performance, as well as the rear wing's individual performance, with smaller corner radii increasing the detriments. For each operating condition, two total downforce enhancement regions were identified along the rear wing's angle of attack range, transitioning around the stall angle. Despite adverse cornering effects, the smallest corner radius marginally extended the rear wing's stall angle.

Downforce losses primarily stemmed from deficits on the underbody and rear wing, alongside increased lift generation on the vehicle's upper surfaces in cornering conditions. Drag penalties mainly resulted from substantial pressure reductions across the vehicle's base surface. Additionally, cornering conditions introduced lateral pressure distribution variations, inducing a centripetal force that increased with reducing corner radii.

The significant pressure reduction on the vehicle's base was due to the formation of a dominant recirculation wake vortex behind the vehicle's inboard side, which intensified at reducing corner radii. However, the enhanced circulation generated by this wake structure also created an inboard inwash of relatively high energy freestream airflow into the wake region, promoting wake dissipation.

Cornering conditions influenced the rear wing's vortical flow, notably affecting the pressure distribution near the endplates. Most significant pressure distribution variations were found on the rear wing's lower surface before reaching its stall angle. This included an initial increase suction on the inboard side at low angles of attack, which transitioned to increased suction levels on the outboard side at higher angles of attack due to intensified vortical flow and enhanced interaction with faster-moving relative airflow.

In each operating condition, the initial vehicle's total downforce enhancement region was mainly due to the rear wing's individual downforce contribution. However, beyond its stall angle, the rear wing's performance declined significantly. At high angles of attack, its pressurisation effect on the vehicle's upper surfaces became the primary mechanism for generating downforce. Nonetheless, at such high angles, the rear wing's interaction with the near-wake resulted in notably higher pressure drag.

15

Overall, this research highlighted the significance of operating conditions on the aerodynamic intricacies of high performance vehicles. The findings offered crucial insights into the complex aerodynamic interactions between the vehicle and its rear wing under varying operating conditions. The analysis of such characteristics does not only endorse the design of static rear wing configurations, but also lays groundwork for the development of sophisticated active designs. Such advancements hold promise for further optimisation of high-performance vehicle aerodynamics and ultimately pushing performance boundaries.

Acknowledgements

Conflict of Interest Statement

The authors have no conflicts to disclose.

Data Availability Statement

Data supporting this study are included within the article.

References

C. Albukrek, P. Doddegowda, A. Ivaldi, J. Amodeo, and E. Bardoscia. Unsteady flow analysis of a formula type open wheel race car in cornering. In *Motorsports Engineering Conference Exposition*. SAE International, dec 2006. doi: https://doi.org/10.4271/2006-01-3661.

J. Broniszewski and J. Piechna. A fully coupled analysis of unsteady aerodynamics impact on vehicle dynamics during braking. *Engineering Applications of Computational Fluid Mechanics*, 13(1):623–641, 2019. doi: 10.1080/19942060.2019.1616326.

J. Broniszewski and J. R. Piechna. Fluid-structure interaction analysis of a competitive car during brake-in-turn manoeuvre. *Energies*, 15(8), 2022. ISSN 1996-1073. doi: https://doi.org/10.3390/en15082917.

A. Buljac, I. Džijan, I. Korade, S. Krizmanić, and H. Kozmar. Automobile aerodynamics influenced by airfoil-shaped rear wing. *International Journal of Automotive Technology*, 17(3):377–385, 2016. doi: https://doi.org/10.1007/s12239-016-0039-4.

K. P. Garry and G. M. Le Good. An investigation of the sensitivity of rear wing orientation for saloon race cars. In *SAE 2005 World Congress & Exhibition*. SAE International, apr 2005. doi: https://doi.org/10.4271/2005-01-1018.

D. Gogel and H. Sakurai. The effects of end plates on downforce in yaw. In *Motorsports Engineering Conference & Exposition*. SAE International, dec 2006. doi: https://doi.org/10.4271/2006-01-3647.

A. Heft, T. Indinger, and N. Adams. Introduction of a new realistic generic car model for aerodynamic investigations. *SAE Technical Paper 2012-01-0168*, 04 2012. doi: https://doi.org/10.4271/2012-01-0168.

E. Josefsson, R. Hagvall, M. Urquhart, and S. Sebben. Numerical analysis of aerodynamic impact on passenger vehicles during cornering. In *CO2 Reduction for Transportation Systems Conference*. SAE International, may 2018. doi: https://doi.org/10.4271/2018-37-0014.

J. Katz and L. Dykstra. Study of an open-wheel racing-car's rear-wing aerodynamics. In *SAE International Congress and Exposition*. SAE International, feb 1989. doi: https://doi.org/10.4271/890600.

J. Katz and R. Largman. Experimental study of the aerodynamic interaction between an enclosed-wheel racing-car and its rear wing. *Journal of Fluids Engineering*, 111(2):154–159, 06 1989. ISSN 0098-2202. doi: https://doi.org/10.1115/1.3243616.

J. Keogh. *The Aerodynamic Effects of the Cornering Flow Conditions*. PhD thesis, School of Mechanical and Manufacturing Engineering, University of New South Wales, 2016.

J. Keogh, T. Barber, S. Diasinos, and G. Doig. Techniques for aerodynamic analysis of cornering vehicles. In *18th Asia Pacific Automotive Engineering Conference*. SAE International, mar 2015a. doi: https://doi.org/10.4271/2015-01-0022.

J. Keogh, G. Doig, S. Diasinos, and T. Barber. The influence of cornering on the vortical wake structures of an inverted wing. *Proceedings of the Institution of Mechanical Engineers, Part D: Journal of Automobile Engineering*, 229 (13):1817–1829, 2015b. doi: 10.1177/0954407015571673.

J. Keogh, T. Barber, S. Diasinos, and G. Doig. The aerodynamic effects on a cornering ahmed body. *Journal of Wind Engineering and Industrial Aerodynamics*, 154:34–46, 2016. ISSN 0167-6105. doi: https://doi.org/10.1016/j.jweia.2016.04.002.

R. Kono, T. Nakashima, M. Tsubokura, Y. Okada, and T. Nouzawa. Aerodynamics simulation of a sedan-type road vehicle in cornering motion with roll angle. In *34th AIAA Applied Aerodynamics Conference*. American Institute of Aeronautics and Astronautics, 2016. doi: https://doi.org/10.2514/6.2016-3726.

K. Kurec, M. Remer, T. Mayer, S. Tudruj, and J. Piechna. Flow control for a car-mounted rear wing. *International Journal of Mechanical Sciences*, 152:384–399, 2019. ISSN 0020-7403. doi: https://doi.org/10.1016/j.ijmecsci.2018.12.034.

M. Lanfrit. Best practice guidelines for handling automotive external aerodynamics with fluent. 2005. Fluent Deutschland GmbH.

A. Mathur, A. Mahajan, A. Aggarwal, C. Mishra, and A. Roy. Numerical study of swan neck rear wing for enhancing stability of ground vehicle bodies. In *Emerging Trends in Mechanical Engineering*, pages 199–208, Singapore, 2021. Springer Singapore. doi: https://doi.org/10.1007/978-981-15-8304-9_14.

F. R. Menter. Two-equation eddy-viscosity turbulence models for engineering applications. *AIAA Journal*, 32(8):1598–1605, 1994. doi: https://doi.org/10.2514/3.12149.

D. L. Milliken, E. M. Kasprzak, L. D. Metz, and W. F. Milliken. *Race Car Vehicle Dynamics - Problems, Answers and Experiments*. SAE International, Warrendale, 1995. ISBN 978-0-7680-1127-2.

T. Nakashima, M. Tsubokura, Y. Okada, T. Nouzawa, R. Kono, and Y. Doi. Aerodynamic characteristics of a road vehicle in steady-state cornering. In *Proceedings of the ASME/JSME/KSME 2015 Joint Fluids Engineering Conference. Volume 1A: Symposia, Part 2*. The American Society of Mechanical Engineers, 2015. doi: https://doi.org/10.1115/AJKFluids2015-17553.

T. Nakashima, H. Mutsuda, T. Kanehira, and M. Tsubokura. Fluid-dynamic force measurement of ahmed model in steady-state cornering. *Energies*, 13 (24), 2020. ISSN 1996-1073. doi: 10.3390/en13246592.

K. Nara, M. Tsubokura, and J. Ikeda. *A Numerical Analysis of Unsteady Aerodynamics of Formula Car During Dynamic Cornering Motion*. 2014. doi: https://doi.org/10.2514/6.2014-3138.

Y. Okada, T. Nouzawa, S. Okamoto, T. Fujita, T. Kamioka, and M. Tsubokura. Unsteady vehicle aerodynamics during a dynamic steering action: 1st report, on-road analysis. In *SAE 2012 World Congress & Exhibition*. SAE International, 2012. doi: https://doi.org/10.4271/2012-01-0446.

J. R. Piechna, K. Kurec, J. Broniszewski, M. Remer, A. Piechna, K. Kamieniecki, and P. Bibik. Influence of the car movable aerodynamic elements on fast road car cornering. *Energies*, 15(3), 2022. ISSN 1996-1073.

S. Rijns, T.-R. Teschner, K. Blackburn, and J. Brighton. Integrated numerical and experimental workflow for high-performance vehicle aerodynamics. *SAE Technical Paper 2024-01-5016*, 2024a. ISSN 0148-7191. doi: https://doi.org/10.4271/2024-01-5016.

S. Rijns, T.-R. Teschner, K. Blackburn, A. Proenca, and J. Brighton. Experimental and numerical investigation of the aerodynamic characteristics of high performance vehicle configurations under yaw conditions [manuscript submitted for publication]. *Advanced Vehicle Engineering Centre, Cranfield University*, 2024b.

J. W. Saunders and R. B. Mansour. On-road and wind tunnel turbulence and its measurement using a four-hole dynamic probe ahead of several cars. In *SAE 2000 World Congress*. SAE International, 2000. doi: https://doi.org/10.4271/2000-01-0350.

R. F. Soares, A. Knowles, S. G. Olives, K. Garry, and J. C. Holt. On the aerodynamics of an enclosed-wheel racing car: An assessment and proposal of add-on devices for a fourth, high-performance configuration of

16

the drivaer model. *SAE Technical Paper 2018-01-0725*, April 2018. doi: https://doi.org/10.4271/2018-01-0725.

M. Szudarek and J. Piechna. Cfd analysis of the influence of the front wing setup on a time attack sports car's aerodynamics. *Energies*, 14(23), 2021. ISSN 1996-1073. doi: https://doi.org/10.3390/en14237907.

W. Toet. Aerodynamics and aerodynamic research in formula 1. *The Aeronautical Journal*, 117(1187):1–26, 2013. doi: https://doi.org/10.1017/S0001924000007739.

M. Tsubokura, Y. Ikawa, T. Nakashima, Y. Okada, T. Kamioka, and T. Nouzawa. Unsteady vehicle aerodynamics during a dynamic steering action: 2nd report, numerical analysis. *SAE International Journal of Passenger Cars - Mechanical Systems*, 5(1):340–357, apr 2012. ISSN 1946-3995. doi: https://doi.org/10.4271/2012-01-0448.

D. Zavala, W. Vicente, R. Esquivel, and M. Salinas-Vazquez. Numerical simulation of the effect of a centripetal wing spoiler on the flow aerodynamics of a sports car. *SAE Technical Paper 2023-01-5032*, 2023. ISSN 0148-7191. doi: https://doi.org/10.4271/2023-01-5032.

2024-04-09

Effects of cornering conditions on the aerodynamic characteristics of a high-performance vehicle and its rear wing

Rijns, Steven

American Institute of Physics (AIP)